AEM
Journals.ASM.org

Analysis of Magnetosome Chains in Magnetotactic Bacteria by Magnetic Measurements and Automated Image Analysis of Electron Micrographs

E. Katzmann,[a,b]* M. Eibauer,[c] W. Lin,[d] Y. Pan,[d] J. M. Plitzko,[b,e] D. Schüler[a]

Ludwig Maximilians University of Munich, Department of Biology I, Planegg-Martinsried, Germany[a]; Max Planck Institute of Biochemistry, Department of Molecular Structural Biology, Planegg-Martinsried, Germany[b]; University of Zurich, Department of Biochemistry, Zürich, Switzerland[c]; Biogeomagnetism Group, Paleomagnetism and Geochronology Laboratory, Key Laboratory of the Earth's Deep Interior, Institute of Geology and Geophysics, Chinese Academy of Sciences, Beijing, China[d]; Bijvoet Center for Biomolecular Research, Utrecht University, Utrecht, The Netherlands[e]

Magnetotactic bacteria (MTB) align along the Earth's magnetic field by the activity of intracellular magnetosomes, which are membrane-enveloped magnetite or greigite particles that are assembled into well-ordered chains. Formation of magnetosome chains was found to be controlled by a set of specific proteins in *Magnetospirillum gryphiswaldense* and other MTB. However, the contribution of abiotic factors on magnetosome chain assembly has not been fully explored. Here, we first analyzed the effect of growth conditions on magnetosome chain formation in *M. gryphiswaldense* by electron microscopy. Whereas higher temperatures (30 to 35°C) and high oxygen concentrations caused increasingly disordered chains and smaller magnetite crystals, growth at 20°C and anoxic conditions resulted in long chains with mature cuboctahedron-shaped crystals. In order to analyze the magnetosome chain in electron microscopy data sets in a more quantitative and unbiased manner, we developed a computerized image analysis algorithm. The collected data comprised the cell dimensions and particle size and number as well as the intracellular position and extension of the magnetosome chain. The chain analysis program (CHAP) was used to evaluate the effects of the genetic and growth conditions on magnetosome chain formation. This was compared and correlated to data obtained from bulk magnetic measurements of wild-type (WT) and mutant cells displaying different chain configurations. These techniques were used to differentiate mutants due to magnetosome chain defects on a bulk scale.

Magnetoaerotaxis of magnetotactic bacteria (MTB) is based on intracellular membrane-enclosed magnetite (Fe_3O_4)/greigite (Fe_3S_4) crystals, the magnetosomes (1). The chain-like arrangement of magnetosomes allows adding up of all the individual magnetic moments, which results in a dipole strong enough to align the cell within the Earth's weak magnetic field. In the alphaproteobacterium *Magnetospirillum gryphiswaldense*, magnetosome biomineralization and chain assembly are under genetic control (2–5) and involve at least 2 known key proteins: the acidic and repetitive MamJ connects the magnetosomes to the cytoskeletal magnetosome filament formed by the actin-like MamK, which assembles and positions the magnetosome chains (MCs) within the cell (6–9). Deletion of both genes, which are adjacent to each other within the *mamAB* operon, resulted in distinct and characteristic phenotypes: Δ*mamJ* strains exhibit clustered magnetosomes whereas Δ*mamK* strains have fragmented chains at ectopic positions which are prone to mispartitioning during cell division (6, 8, 10, 11). In addition to biological control, concatenation of nascent magnetosome crystals is further governed by magnetic attraction forces within the chain (12). Individual magnetic moments of the magnetite crystals contribute to chain formation by short-range (<50-nm) magnetic interactions (9, 12–14) but are alone not sufficient to align and position the MCs at their typical midcell location. Moreover, positioning, division, and equipartitioning of MCs during cell division of *M. gryphiswaldense* is dependent on MamK (9).

However, beside the dedicated functions for chain assembly provided by MamJ and MamK, physical properties (i.e., size, shape, and, consequently, magnetization) of magnetite crystals also depend on other factors controlling biomineralization (3), as well as on growth conditions (9, 12–18). For example, increasing oxygen concentrations gradually impaired biomineralization in *M. gryphiswaldense* (16, 19, 20). Deletion of the *nap* genes involved in denitrification redox control in *M. gryphiswaldense* showed severely impaired magnetite biomineralization and resulted in smaller crystals that were poorly aligned in irregular chains (21). Besides, other environmental factors affecting growth have not been systematically tested (17). Previous attempts to study and quantify chain assembly by magnetic orientation (Cmag) and transmission electron microscopy (TEM) analysis were straightforward and sufficient for *M. gryphiswaldense* wild-type (WT) strains and the few available MC mutants. However, since other, recently described phenotypes displayed more subtle defects in MC assembly, simple Cmag measurements proved too insensitive to resolve quantitative differences. On the other hand, TEM data analysis is tedious, time-consuming, and limited by the need of manual evaluation.

Therefore, in this study we first identified growth conditions optimal for MC formation. MC assembly was then quantitatively

Received 29 June 2013 **Accepted** 30 September 2013
Published ahead of print 4 October 2013

Address correspondence to D. Schüler, dirk.schueler@bio.lmu.de.
* Present address: E. Katzmann, JEOL (Germany) GmbH, Eching, Germany.

Supplemental material for this article may be found at http://dx.doi.org/10.1128/AEM.02143-13.

doi:10.1128/AEM.02143-13

assessed by a novel tool, the chain analysis program (CHAP) developed in this study to improve and facilitate image analysis of MCs in *M. gryphiswaldense* TEM micrographs. To test whether the results obtained by single-cell analysis can be correlated to data from bulk samples, magnetic domain state investigation techniques were applied and compared with measurements by the classical light-scattering assay for magnetospirilla (Cmag) (22).

MATERIALS AND METHODS

Bacterial strains and cultivation procedures. *M. gryphiswaldense*, a Δ*mamJ* mutant, a Δ*mamK* mutant, and *M. gryphiswaldense* strain B were routinely grown under anoxic conditions at 20°C in modified FSM medium or in LIM (low-iron media; modified FSM medium) using moderate shaking (120 rpm) as described previously (19, 20, 23).

Nonmagnetic *M. gryphiswaldense* WT cells were grown under various abiotic conditions: temperatures of 15°C, 20°C, 25°C, 30°C, and 35°C and oxic (~21% O_2), microoxic (2% O_2), and anoxic (0 to 0.5% O_2) oxygen concentrations. Cells were cultured in Hungate vials to an optical density at 565 nm (OD_{565}) of 1 to 1.6. For lower temperatures (e.g., 15°C), incubation periods of up to 8 days were necessary. Growth curves were recorded for each set of conditions. For TEM examination, cells were harvested after 8 days at 15°C, 23 to 30 h at 20°C, and 23 h at 25°C, 30°C, and 35°C. The cells were then inactivated by the addition of paraformaldehyde (Fluka, Switzerland) to reach a final concentration of 0.1% before the measurement and TEM analyses were performed as described elsewhere (8).

Rock magnetic measurements. All 4 strains were grown for 2 passages under 20°C anoxic conditions in FSM medium supplemented with 8 mM $NaNO_3$ in Hungate vials. Subsequently, 20 ml was used as an inoculum for a 500-ml culture in rubber-plug-sealed glass bottles and incubated without shaking (static conditions). Cells were harvested by centrifugation after 60 h of growth with an optical density of ~0.66 and a magnetic response of 0 (*M. gryphiswaldense* strain B), 0.7 (Δ*mamJ* mutant), 1.3 (WT strain), or 1.6 (Δ*mamK* mutant). For subsequent analysis, cells were preserved with formaldehyde (2 μl/ml of 36.5% paraformaldehyde stock solution [7]) and stored at 4°C. Optical densities and C_{mag} values of *M. gryphiswaldense* cultures were measured turbidimetrically at 565 nm with immotile cells inactivated by the addition of paraformaldehyde (see above) prior to the measurement.

TEM analysis. For conventional transmission electron microscopy (TEM) analysis, unstained cells were adsorbed on carbon-coated copper grids (Plano, Wetzlar, Germany). Bright-field TEM was performed using an FEI Tecnai F20 transmission electron microscope (FEI Company, Eindhoven, The Netherlands) at an accelerating voltage of 200 kV. Images were captured with an Eagle charge-coupled-device (CCD) camera (4,096 × 4,096 pixels) using EMMenue 4.0 (Tietz, Gauting, Germany) and FEI software. TEM micrographs were usually acquired at 6,500-fold magnification, a defocus of −8 μm, and an object pixel size of 1.672 nm/pixel. TEM images were binned, and 2 pixels correspond to 3.3 nm. The resolution of the images is limited to 4.5 nm.

CHAP (chain analysis program). In a first step, the cell membrane and magnetite crystals of the TEM micrograph files were manually segmented with Photoshop (Adobe CS 4 Extended, version 11.0.2; Adobe Systems, Inc.). All subsequent procedures were implemented in Matlab (Matlab2012a; TheMathWorks, Inc.) by custom-written scripts. From the segmented cell membrane, the cell area was calculated, and from the segmented magnetite crystals, their number per chain and their corresponding radii and standard deviations were determined. Next, the center of gravity of the magnetosome chains was calculated and along with the cell membrane shifted to the point of origin. This was in preparation for magnetosome chain orientation calculations. Therefore, the shifted magnetosome chain was mirrored along the *y* axis and rotated until it matched the original (shifted) chain (24).

The rotation angle divided by 2 resulted in the angle along which the chain was oriented along the *y* axis. This angle was subsequently inversely applied to the membrane and magnetosome chain. As a result, a cell with a *y* axis-oriented magnetosome chain with its center of gravity in the point of origin was generated. These pretreated cells were summed to generate composite images under the different abiotic conditions.

For heat-plot representation, aligned magnetosome chains were used and each magnetite crystal was given a value of 1. The intensity of a certain pixel corresponds to the number of magnetite crystals within this pixel. The corresponding colors range from blue (no magnetite) to dark red (250 magnetite crystals [maximum value]). The color spectrum is a result of the different magnetite particle numbers/pixel.

Magnetic measurements. For magnetic measurements, all samples were separately harvested by centrifuging at 4°C. Cell samples were then carefully placed into nonmagnetic gelatin capsules and were dried overnight in a Coy anoxic chamber (Coy Laboratories, Ann Arbor, MI).

Room temperature magnetic measurements were performed on a model 3900 vibrating sample magnetometer (VSM MicroMag 3900; Princeton Measurement Corporation). Hysteresis loops were measured at levels ± 500 mT. Saturation magnetization (M_s), saturation remanence (M_{rs}), and coercivity (B_c) were characterized after the high-slope paramagnetic correction. The coercivity of remanence (B_{cr}) was acquired by measuring the back-field demagnetization curve. For each sample, first-order reversal curves (FORCs) were measured with an increasing field step (δH) of 1.16 mT and an averaging time of 150 ms. The smoothing factors of the *M. gryphiswaldense* WT, Δ*mamK*, and Δ*mamJ* strains were 2.7, 2.7, and 3.6, respectively.

Low-temperature magnetic properties were measured by using a Quantum Design magnetic property measurement system (MPMS-XL-5; Quantum Designs). Samples were cooled to 10 K in a zero-field environment (using zero-field cooling [ZFC]) and then saturated by applying a 2.5-T field. After the applied field was removed, the thermal demagnetization curve was measured at 10 to 300 K. The sample was cooled from 300 to 10 K in the presence of a 2.5-T field (field cooling [FC]), and the thermal demagnetization curves was measured in the zero-field environment during warming to 300 K. The Verwey transition temperature (T_v) for each sample was determined at the point which the dM/dT is maximum. The delta ratio (δ_{FC}/δ_{ZFC}) was calculated from FC and ZFC curves according to reference 25, i.e., δ_{FC} (and δ_{ZFC}) was calculated as $\delta = (M_{80K} - M_{150K})/M_{80K}$, where M_{80K} and M_{150K} are the remanences measured at 80 K and 150 K, respectively (26).

RESULTS

Analysis of growth conditions affecting MC formation. Cells of the *M. gryphiswaldense* WT strain were grown under different conditions, and chain formation was assessed with respect to (i) magnetite crystal morphology and (ii) magnetosome size and number as well as (iii) MC length. Initially, the magnetic orientation of *M. gryphiswaldense*, as measured by Cmag (the ratio of scattering intensities at different angles of a magnetic field relative to a light source [22]), and growth were determined in three independent trials using cultures grown under oxic, microoxic (mic), or anoxic conditions between 15°C and 35°C (Fig. 1).

While there was no significant growth below 15°C and above 35°C, growth at moderate temperatures reached the stationary phase after 23 h at 30°C and 35°C and after 8 days at 15°C (Fig. 1). The oxygen concentration had only a minor influence on cell growth, with lower cell densities under oxic conditions (Fig. 1). Although growth was slightly lower than that seen at 30°C (19), the highest particle numbers and most regular crystals were observed at 20°C under anoxic conditions.

TEM of magnetite crystals from ~400 individual cells (>10,000 particles) revealed a Gaussian-like crystal size distribution at low and moderate temperatures (15°C to 30°C) and a decreasing mean diameter at increasing temperatures (~44.7 nm at

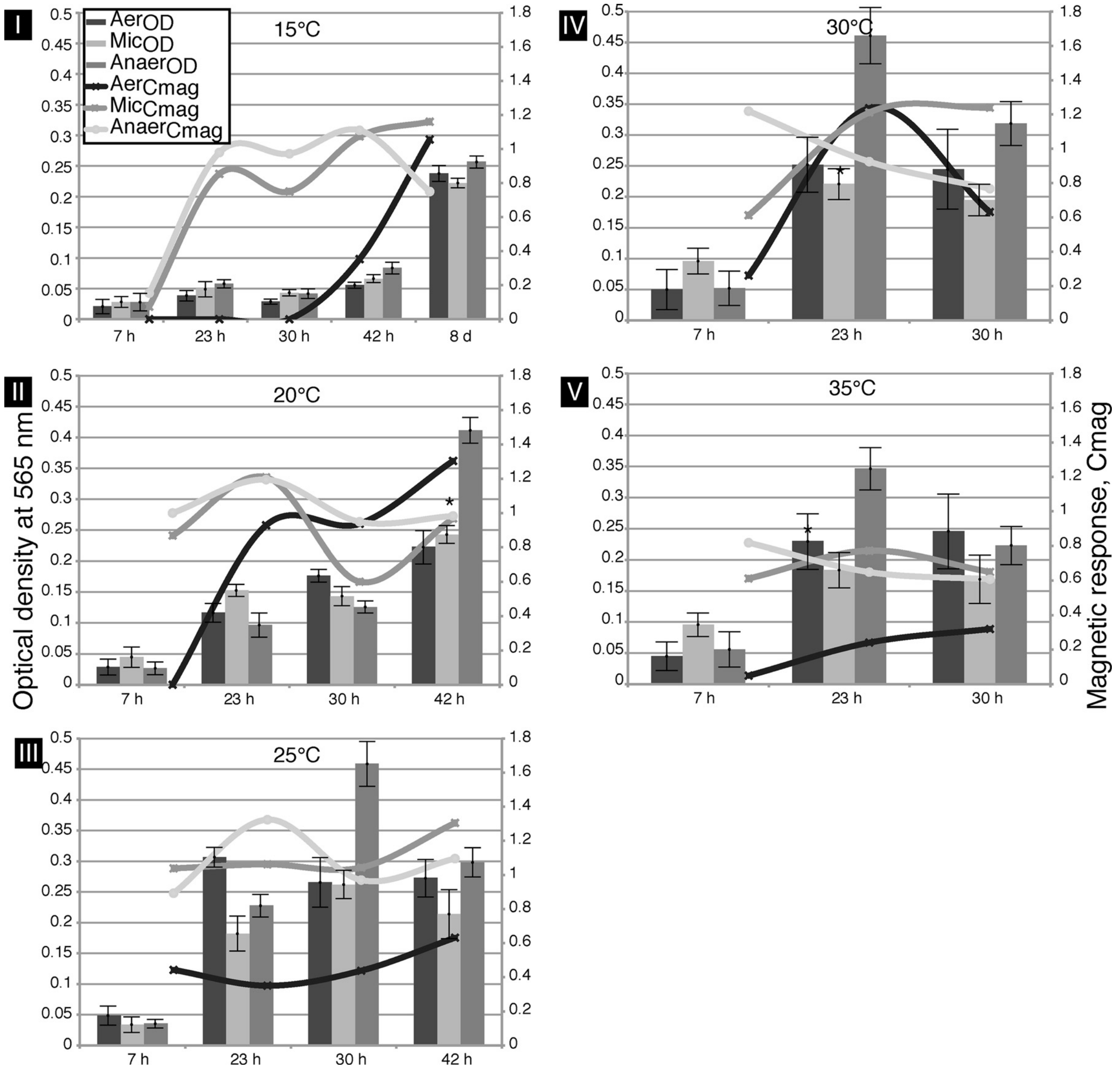

FIG 1 Effects of different oxygen concentrations and temperatures on growth (OD; bars) and magnetic orientation (Cmag; lines) of *M. gryphiswaldense* WT cells over time in magnetic spirillum growth medium (MSGM). (I) Cells were incubated at 15°C for up to 8 days and analyzed at 5 time points. Under microoxic (mic) and anoxic (anox) conditions, biomineralization occurred within 24 h. Oxic (ox) biomineralization started after a delay of 42 h. Stationary phase was reached after 8 days. (II and III) Magnetic orientation at 20°C and 25°C under mic or anox conditions was invariant over time. Stationary phase was reached after 42 h (20°C) or 30 h (25°C). (IV and V) At 30°C and 35°C, the stationary-growth phase was reached after 23 h with invariant magnetic orientation. The asterisks denote the corresponding TEM micrographs in Fig. 2I.

20°C and ~29 nm at 35°C) during anoxic growth in three independent trials (Fig. 2). With increasing temperature, crystal shape became more irregular, and twinned or polycrystalline crystal morphologies were prevalent, with diameters of 5 to 15 nm in loosely spaced, short MCs (Fig. 2I and IV). Therefore, we chose anoxic conditions and 20°C for all subsequent analyses of MC formation.

Development of an automated *ch*ain *a*nalysis *p*rogram (CHAP). For quantitative and unbiased studies of MC assembly in *M. gryphiswaldense*, large microscopy data sets have to be analyzed. We therefore developed CHAP as a versatile and high-throughput tool to access parameters of MC position and length as well as particle number and diameter. A regular WT *M. gryphiswaldense* MC was defined as having 10 or more magnetosomes in a row interspaced by gaps not larger than ~50 nm and a particle diameter of at least 20 nm. The chain axis was defined by the interspacing threshold of the individual particles, and adjacent crystals should not deviate by more than 90° from the long axis (8).

CHAP recognizes cells and MCs in preprocessed TEM micrographs in which cell boundaries and MCs are segmented as different layers represented by levels of gray shading. The program then analyzes segmented micrographs by Matlab algorithms (Matlab2012a; TheMathWorks, Inc.). Different parameters such as chain position and crystal number and size can be determined and visualized as graphs, composite images, and heat plots. To compare this data set with manually examined TEM data sets, ~20 cells from each TEM micrograph per condition were exam-

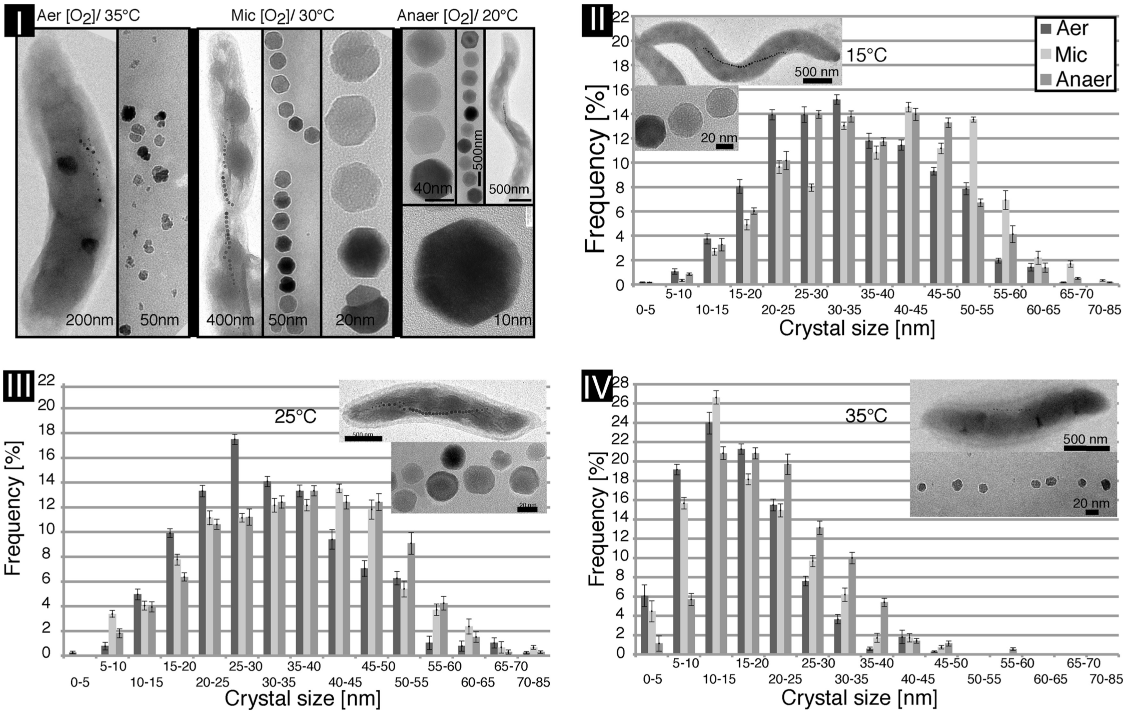

FIG 2 Effect of oxygen and temperature on magnetosome chain (MC), magnetite crystal size, and morphology. (I) TEM micrograph panel of *M. gryphiswaldense* WT cells and their corresponding MCs and details of crystals under ox (35°C), mic (30°C), and anox (20°C) conditions. (II to IV) Magnetite crystal diameters (gray bars) of ~350 analyzed particles per condition. Increase in temperature results in higher frequencies of small magnetite crystals (dark gray, ox; light gray, mic; medium gray, anox). Aer, aerobic; Anaer, anaerobic.

ined by the CHAP algorithm (in total, ~400 cells). To this end, different representations of aligned MCs and crystal number and diameter as well as heat maps for MC localization in *M. gryphiswaldense* were generated (Fig. 3; see also Fig. S1 in the supplemental material). In addition, the automated analysis of an overlay array of all cells around their center revealed that the cell length decreased with increasing temperature (Fig. 3I to II). When individual MCs of these cells were aligned around their center by CHAP, it became even more evident that oxygen concentration and temperature significantly affected the number of crystals in MCs and, as a result, the extension of the latter. Cuboctahedron-shaped crystal morphology observed by TEM became less regular under oxic conditions with high temperatures. Both conditions caused the strongest perturbances, resulting in short MCs (~13 crystals/chain at 35°C) compared to MCs of cells grown under anoxic conditions at 20°C (~45 crystals/chain). CHAP also revealed the average cell area. An increase of cell area (as a proxy for cell volume) was caused by a decreasing growth temperature (~2.1 μm^2 at 35°C and ~2.7 μm^2 at 15°C) (Fig. 3I to II).

Cell size and the number of crystals per MC were poorly correlated when plotted against each other (Fig. 3II) (correlation coefficient = 0.33; coefficient of determination = 0.11). This is in contrast to previous observations on cephalexin-treated, division-inhibited cells, in which long (on average, 25.6-μm) filamentous cells had MCs with up to 224 magnetite crystals (9). However, in the majority (78%) of analyzed cells, magnetite crystal numbers were rather invariant (~30 ± 10 particles), and the invariance was independent of cell size variations (minimum, 1.74 μm^2; maximum, 3.03 μm^2), with the exception of small MCs and cells at 35°C (Fig. 3I to II). Under anoxic conditions, particles were largest, at 42.4-nm diameter on average (28.4 nm to 31.5 nm under oxic to microoxic conditions in three independent trials), whereas the inhibiting effect of oxygen on crystal size was less pronounced at low growth rates (e.g., at 15°C) (Fig. 3III). This demonstrates that oxygen and temperatures above 30°C cause the formation of scattered, widely spaced, loosely arranged, and shorter MCs compared to the tightly spaced, almost linear long chains found under optimum conditions.

CHAP analysis of MC-impaired mutants. CHAP was further used to analyze genetic effects on MC configurations. We chose *M. gryphiswaldense* mutant strains Δ*mamK* and Δ*mamJ* because of their known MC phenotypes (6, 8). *M. gryphiswaldense* strain B, a spontaneous mutant lacking most magnetosome genes, served as a control because of its inability to synthesize any magnetosome-like particles (5). While the majority of Δ*mamJ* cells formed magnetosome clusters as described before (6, 7), we identified a small portion of Δ*mamJ* cells (<10%) in which short chains, rings, and even parallel chains were apparent (see Fig. S1 in the supplemental material). Short chains mostly consisted of fewer than 10 magnetosomes and were randomly positioned within the cell (Fig. S1). However, individual magnetosomes apart from the cluster were also observed (Fig. 3IV).

The Δ*mamK* deletion mutant displayed fragmented chains with multiple subchains at ectopic positions as expected (Fig. 3IV) (8). CHAP alignment of the individual short-chain fragments to the cell center (Fig. 3V) clearly showed that the MCs in the Δ*mamK* mutant were significantly shorter than in WT cells (see Fig. S2 in the supplemental material).

Rock magnetic measurements. First-order reversal curve, hysteresis loop, and saturated isothermal remanence magnetiza-

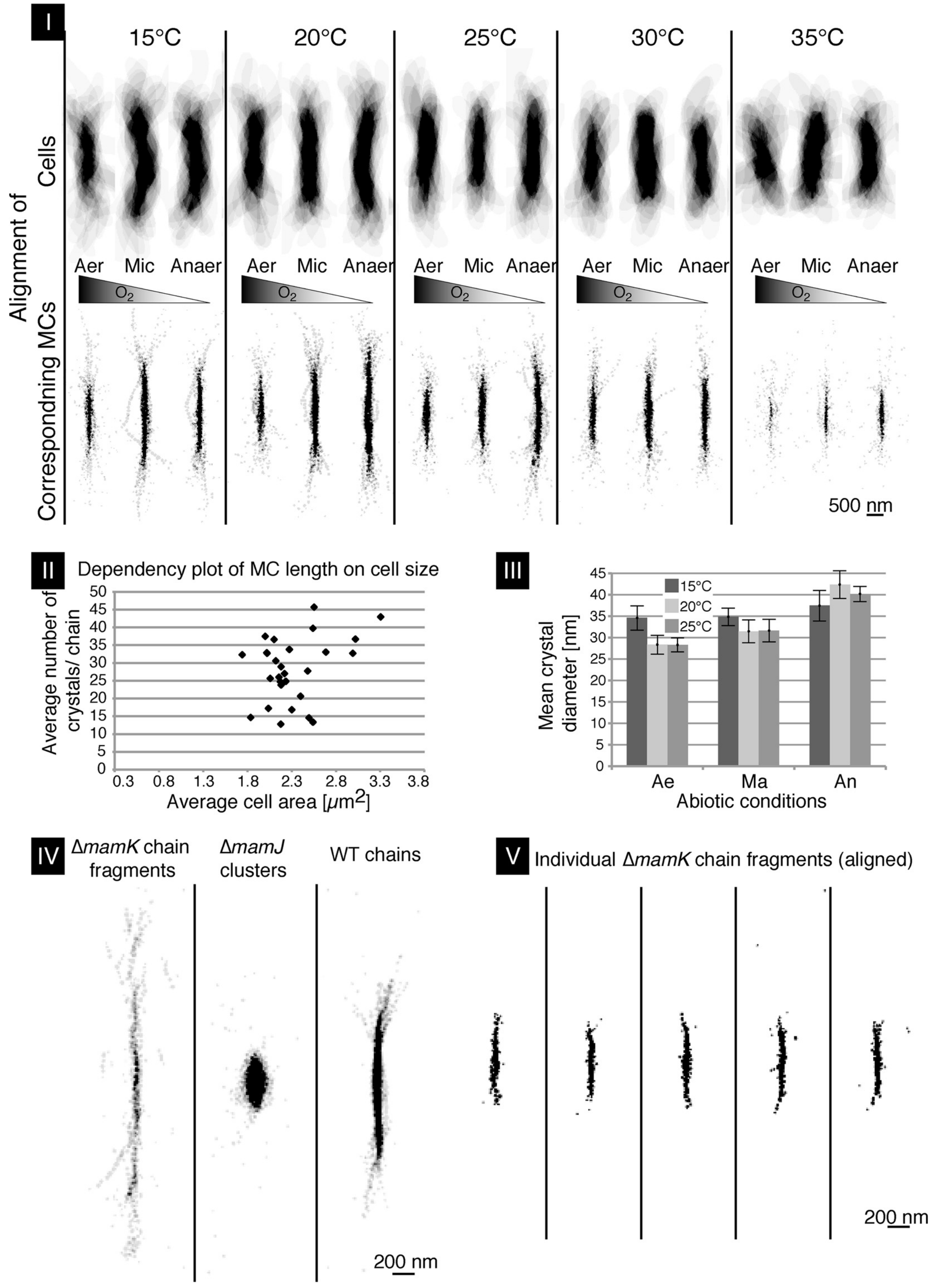

FIG 3 Chain length, position, and location in *M. gryphiswaldense* cells as revealed by CHAP. (I) CHAP-analyzed WT cells at different temperatures and oxygen concentrations. Center alignment of ~20 cells per condition (upper panel) with corresponding MCs (lower panel) at decreasing [O_2] levels (center, left to right) is shown. (II) Plot of *M. gryphiswaldense* cell area against crystal number per chain. (III) Mean magnetosome crystal diameter at lower temperatures under ox to anox conditions. Ae, aerobic; Ma, microaerobic; Ar, anaerobic. (IV) Aligned MCs and clusters analyzed as described for Fig. 4 were CHAP aligned to cell centers of *M. gryphiswaldense* Δ*mamK*, Δ*mamJ*, and WT. (V) CHAP-analyzed MCs of 25 Δ*mamK* cells in which fragmented subchains were recognized as independent chains. Five analyzed TEM micrographs of Δ*mamK* cells and their cell center-aligned MC fragments are shown. The cells shown in panels IV and V were grown at 20°C under anox conditions.

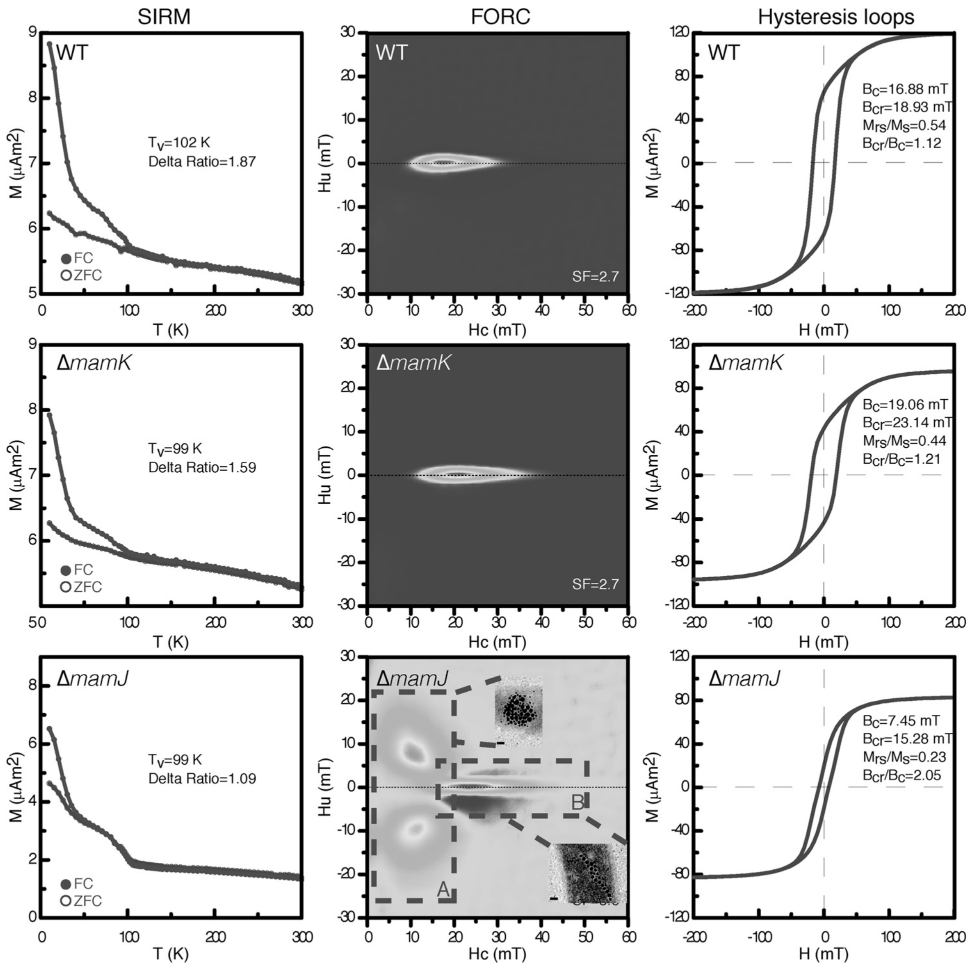

FIG 4 Low-temperature remanence demagnetization, room-temperature first-order reversal curves (FORC), and hysteresis loops determined with bulk samples of *M. gryphiswaldense* WT, Δ*mamJ*, and Δ*mamK* grown under anox conditions at 20°C. Remanence demagnetization curves (left) after FC (field cooling) and ZFC (zero field cooling) treatments are shown. Tv, the Verwey transition temperature. Delta ratio, δ_{FC}/δ_{ZFC} [here, $\delta = (J_{80K} - J_{150K})/J_{80K}$; J_{80K} and J_{150K} represent remanence at 80 K and 150 K, respectively]. The FORC diagrams (center) represent the MC configuration of the individual cultures. *x* axis, distribution of coercivity; *y* axis, distribution of magnetic interaction between particles. Dashed boxes A and B highlight distinctive features of the mutant Δ*mamJ* FORC pattern. Room-temperature hysteresis loops (right) of *M. gryphiswaldense* samples are shown. M (µA·m^2), magnetic moment; Hu (mT), bias field; Hc (mT), coercivity; H (mT), magnetic field; M_s, saturation magnetization; M_{rs}, saturation remanence; B_c, coercive force; B_{cr}, coercivity of remanence.

tion (SIRM) studies were recently employed to investigate MC formation in WT MTB (18, 27, 28). We conducted similar experiments on our mutant strains impaired in MC formation (6, 8, 10, 11, 29) to validate the most prominent MC configurations and correlate the "fingerprints" obtained from bulk measurements.

FORC, hysteresis loop, and low-temperature demagnetization measurements were applied to the *M. gryphiswaldense* WT strain, the Δ*mamK* mutant, the Δ*mamJ* mutant, and nonmagnetic *M. gryphiswaldense* strain B grown anoxically at 20°C. Low-temperature demagnetization measurements allow the detection of MCs in bulk samples and are commonly applied to sediment samples as well as MTB cells (30–32). Except for the control (nonmagnetic *M. gryphiswaldense* strain B; not shown), all samples (the WT, Δ*mamK*, and Δ*mamJ* strains) exhibited a Verwey transition with a temperature between 99 and 103 K, similar to other published results for MTB (86 to 117 K) (17, 18) (Fig. 4). The delta ratio, a measurement of the amount of remanence lost upon warming through the Verwey transition, of these three samples was lower than 2. Interestingly, the delta ratio of the *M. gryphiswaldense* WT strain (1.87) was higher than that of the Δ*mamK* mutant (1.59), and the delta ratio of the Δ*mamK* mutant was higher than that of the Δ*mamJ* mutant (1.09), indicating the more regular chain structure of the WT strain compared to the Δ*mamK* mutant and of the Δ*mamK* mutant compared to the Δ*mamJ* mutant (Fig. 4, left panel). Thus, these bulk data confirm previous TEM observations (6, 8).

To test whether the magnetic properties of disturbed MCs can be distinguished from those of the WT MCs, FORC diagrams were obtained for Δ*mamJ* and Δ*mamK* mutant cultures. The FORC diagrams (Fig. 4, center) of WT and Δ*mamK* mutant samples were very similar, representing a narrow distribution in the vertical direction and elongation along the horizontal axis and indicating single-domain (SD) particles in a chain arrangement with weak interactions. The Δ*mamK* mutant sample had slightly higher coercivity than the WT sample. The signals from the two types were almost indistinguishable. However, the FORC of the Δ*mamJ* mutant is remarkable: one region (Fig. 4, center bottom [inset A]) was composed of 2 peaks, which is previously described only for pseudo-single-domain (PSD) magnetite particles at low temperatures (20 to 95 K) (33) and is shown in MTB cells for the first time here. We noted that region B was comparable to that in WT and Δ*mamK* mutant samples, suggesting that a proportion of Δ*mamJ* mutant cells contained chain-like structures or fragmented chains of magnetosomes, consistent with CHAP/TEM data (Fig. 3 and 4; see also Fig. S1 in the supplemental material).

Room temperature hysteresis loops of all samples (*M. gryphiswaldense* strain B not shown) are presented in Fig. 4. The WT, Δ*mamJ*, and Δ*mamK* strains showed the typical pattern for magnetite. All samples were saturated at a field of ~50 to 100 mT. The coercive force (B_c) and coercivity of remanence (B_{cr}) values for the Δ*mamK* mutant were slightly higher than those for the WT strain, while the B_c and B_{cr} values for the Δ*mamJ* mutant were apparently lower than those of the Δ*mamK* mutant as well as WT cells. The remanence and coercivity ratios (M_{rs}/M_s and B_{cr}/B_c) suggest that the magnetosomes in the WT and Δ*mamK* strains are SD particles whereas the magnetosomes in the Δ*mamJ* mutant have shown a PSD behavior.

DISCUSSION

In this study, we established growth conditions for the optimal formation of MCs. Our report confirms previous studies with respect to the influence of oxygen and aeration on growth and biomineralization (17, 19). Likewise, we demonstrated that increasing the temperature has an inhibitory effect on biomineralization and, consequently, MC assembly. The observed defects could have been caused by general heat stress or might have resulted from the direct effect of temperature on membrane properties such as altered fluidity and lipid composition (13) that may also affect biomineralization in magnetosome membranes.

Additionally, we developed a new MC analysis tool and used it to characterize mutants impaired in MC formation. Applying the CHAP algorithm to MTB has significant advantages over manual TEM micrograph examination: automated CHAP allows the study of MC assembly quantitatively, without the bias caused by manual analysis. The alignment of individual chains allowed visualization of the probability density for the magnetite particles according to changing parameters. The tool further enables the convenient and simultaneous determination of multiple parameters such as particle number, particle size, and MC length and position within the cell as well as cell dimensions (i.e., length, diameter, and area).

With minor adaptations, CHAP can be also applied to other species of magnetosome-forming MTB, which display a great variety of magnetosome sizes, shapes, and numbers as well as chain organization characteristics (34). However, intensity segmentation largely depends on the quality and number of TEM micrographs and is the time-limiting step. A stable defocus is recommended to reduce defocus fringes around the magnetite, which complicate measurements of crystal size or intensity segmentation. We also simulated the influence of the contrast transfer function (ctf) on the intensity segmentation of the magnetosomes on TEM micrographs. The ctf was applied with the actual acquisition parameter set to a 20-pixel (33.44-nm diameter) magnetosome crystal model. Again, we measured a diameter of 20 pixels by intensity segmentation, which confirmed that the influence of the ctf is insignificant at the magnification and defocus chosen for acquisition of TEM micrographs for CHAP analysis (see Fig. S3 in the supplemental material). However, intensity segmentation accuracy ranged between ±2 pixels (i.e., ±3.3 nm), which is below the resolution of the TEM micrographs. The upper intensity segmentation error is thus defined by the micrograph resolution of 4.5 nm and the error of ±3.3 nm. To distinguish magnetosomes from debris or artifacts, the cell boundary (i.e., cell membrane) was intensity segmented and used as a mask to analyze the enclosed magnetosomes.

The data obtained by low-temperature magnetic measurements correlate well with the observations made by conventional TEM and CHAPS analysis but not with those made by simple Cmag analysis (6, 8, 35). For the first time, low-temperature demagnetization showed by the decreasing delta ratio values between the WT (1.87), Δ*mamK* (1.59), and Δ*mamJ* (1.09) strains that this method may be suitable to detect MC defects, as we interpret these values (Fig. 4, left). The differences between these three samples, e.g., in delta ratio and T_v values, are possibly due to the chain structure and/or to magnetic interaction between magnetosomes. However, we noted that the delta ratios of these three samples were lower than 2, which is inconsistent with most published results from other MTB studies. A delta ratio greater than 2 was supposed to be a criterion for the identification of magnetite magnetosomes in a chain structure (25, 26). The low delta ratio for the *M. gryphiswaldense* WT strain was previously reported and was interpreted as representing nonstoichiometry of magnetite magnetosomes (36). Despite this, the low-temperature magnetic technique is a bulk measurement method comparable to the conventional measurements of magnetic orientation (Cmag), which are quick and simple to use but of only limited resolution and difficult to quantify. The Cmag data correlate with the CHAP and rock magnetic measurement data, but Cmag analysis is not nearly as sensitive as CHAP analysis in terms of MC configuration determinations. Moreover, no further information about magnetic interactions in a MC is revealed.

The FORC diagrams of *M. gryphiswaldense* WT and Δ*mamK* mutant cells are very similar, representing the SD magnetite distribution and weak magnetic interaction (Fig. 4, center). Surprisingly, the FORC results from the short, fragmented Δ*mamK* mutant chains seemed to be indistinguishable from the WT FORC results, possibly due to significant magnetic contributions of the fragmental chains in the Δ*mamK* mutant. The FORC data obtained from the Δ*mamJ* mutant are of particular interest. To our knowledge, the pattern detected in region A of the Δ*mamJ* mutant (Fig. 4, center) is observed for MTB at room temperature for the first time here, and currently we do not know how to explain it. Possibly, the strong interactions between individual magnetosome particles within the clusters together with a small amount of short or parallel chains of magnetosomes in Δ*mamJ* mutant cells might cause this irregular pattern.

In the hysteresis loop analyses (Fig. 4, right), we noticed that the B_c and B_{cr} values of the Δ*mamK* mutant are slightly higher than those of the WT strain. This is probably due to differences in particle sizes and/or magnetic interactions. The B_c and B_{cr} values of the Δ*mamJ* mutant, however, are apparently lower than those of the Δ*mamK* mutant cells as well as those of the WT cells. We suppose that the strong interactions between magnetosomes in the Δ*mamJ* mutant sample may reduce the coercive force and coercivity.

In conclusion, we introduced additional tools for MC analysis which together provide unprecedented sensitivity and resolution. The combination of TEM and CHAP was used to efficiently determine a variety of MC parameters, which are supported by rock magnetic measurements that complement the analysis by physical parameters of the magnetite crystals. In the future, this might for example allow efficient screening of a multitude of MC mutant phenotypes in various MTB or estimation of variations in MC configurations in entire populations.

ACKNOWLEDGMENTS

This work was funded by the Deutsche Forschungsgemeinschaft (Schu1080/9-1 and -15-1) and the European Union (Bio2Man4MRI).

We thank Günter Pfeifer of the Max Planck Institute of Biochemistry and all members of the Magnetolab.

REFERENCES

1. **Frankel RB, Williams T, Bazlinski D.** 2006. Magneto-aerotaxis, p 1–24. *In* Schüler D (ed), Magnetoreception and magnetosomes in bacteria, 3rd ed, vol 3. Springer Verlag, Berlin, Germany.
2. **Grünberg K, Müller E-C, Otto A, Reszka R, Linder D, Kube M, Reinhardt R, Schüler D.** 2004. Biochemical and proteomic analysis of the magnetosome membrane in *Magnetospirillum gryphiswaldense*. Appl. Environ. Microbiol. **70:**1040–1050.
3. **Lohsse A, Ullrich S, Katzmann E, Borg S, Wanner G, Richter M, Voigt B, Schweder T, Schüler D.** 2011. Functional analysis of the magnetosome island in *Magnetospirillum gryphiswaldense*: the *mamAB* operon is sufficient for magnetite biomineralization. PLoS One **6:**e25561. doi:10.1371/journal.pone.0025561.
4. **Murat D, Quinlan A, Vali H, Komeili A.** 2010. Comprehensive genetic dissection of the magnetosome gene island reveals the step-wise assembly of a prokaryotic organelle. Proc. Natl. Acad. Sci. U. S. A. **107:**5593–5598.
5. **Ullrich S, Kube M, Schübbe S, Reinhardt R, Schüler D.** 2005. A hypervariable 130-kilobase genomic region of *Magnetospirillum gryphiswaldense* comprises a magnetosome island which undergoes frequent rearrangements during stationary growth. J. Bacteriol. **187:**7176–7184.
6. **Scheffel A, Gruska M, Faivre D, Linaroudis A, Graumann PL, Plitzko JM, Schüler D.** 2006. An acidic protein aligns magnetosomes along a filamentous structure in magnetotactic bacteria. Nature **440:**110–114.
7. **Scheffel A, Schüler D.** 2007. The acidic repetitive domain of the *Magnetospirillum gryphiswaldense* MamJ protein displays hypervariability but is not required for magnetosome chain assembly. J. Bacteriol. **189:**6437–6446.
8. **Katzmann E, Scheffel A, Gruska M, Plitzko JM, Schüler D.** 2010. Loss of the actin-like protein MamK has pleiotropic effects on magnetosome formation and chain assembly in *Magnetospirillum gryphiswaldense*. Mol. Microbiol. **77:**208–224.
9. **Katzmann E, Müller FD, Lang C, Messerer M, Winklhofer M, Plitzko JM, Schüler D.** 2011. Magnetosome chains are recruited to cellular division sites and split by asymmetric septation. Mol. Microbiol. **82:**1316–1329.
10. **Komeili A, Li Z, Newman D, Jensen G.** 2006. Magnetosomes are cell membrane invaginations organized by the actin-like protein MamK. Science **311:**242–245.
11. **Draper O, Byrne ME, Li Z, Keyhani S, Barrozo JC, Jensen G, Komeili A.** 2011. MamK, a bacterial actin, forms dynamic filaments in vivo that are regulated by the acidic proteins MamJ and LimJ. Mol. Microbiol. **82:**342–354.
12. **Klumpp S, Faivre D.** 2012. Interplay of magnetic interactions and active movements in the formation of magnetosome chains. PLoS One **7:**e33562. doi:10.1371/journal.pone.0033562.
13. **Kalirai SS, Bazylinski DA, Hitchcock AP.** 2013. Anomalous magnetic orientations of magnetosome chains in a magnetotactic bacterium: *Magnetovibrio blakemorei* strain MV-1. PLoS One **8:**e53368. doi:10.1371/journal.pone.0053368.
14. **Simpson ET.** 2008. Electron holography of isolated and interacting magnetic nanocrystals. Doctoral thesis. University of Cambridge, Cambridge, United Kingdom.
15. **Blakemore RP, Short KA, Bazylinski DA, Rosenblatt C, Frankel RB.** 1985. Microaerobic conditions are required for magnetite formation within *Aquaspirillum magnetotacticum*. Geomicrobiol. J. **4:**53–71.
16. **Faivre D, Menguy N, Posfai M, Schüler D.** 2008. Environmental parameters affect the physical properties of fast-growing magnetosomes. Am. Mineral. **93:**463–469.
17. **Popa R, Fang W, Nealson KH, Souza-Egipsy V, Berquó TS, Benerjee SK, Penn LR.** 2009. Effect of oxidative stress on the growth of magnetic particles in *Magnetospirillum magneticum*. Int. Microbiol. **12:**49–57.
18. **Li J, Pan Y.** 2012. Environmental factors affect magnetite magnetosome synthesis in *Magnetospirillum magneticum* AMB-1: implications for biologically controlled mineralization. Geomicrobiol. J. **29:**362–373.
19. **Heyen U, Schüler D.** 2003. Growth and magnetosome formation by microaerophilic *Magnetospirillum* strains in an oxygen-controlled fermentor. Appl. Microbiol. Biotechnol. **61:**536–544.
20. **Faivre D, Böttger LH, Matzanke BF, Schüler D.** 2007. Intracellular magnetite biomineralization in bacteria proceeds by a distinct pathway involving membrane-bound ferritin and an iron(II) species. Angew. Chem. Int. Ed. Engl. **46:**8495–8499.
21. **Li Y, Katzmann E, Borg S, Schüler D.** 2012. The periplasmic nitrate reductase Nap is required for anaerobic growth and involved in redox control of magnetite biomineralization in *Magnetospirillum gryphiswaldense*. J. Bacteriol. **194:**4847–4856.
22. **Schüler D, Uhl R, Bäuerlein E.** 1995. A simple light scattering method to assay magnetism in *Magnetospirillum gryphiswaldense*. FEMS Microbiol. Lett. **132:**139–145.
23. **Lang C, Schüler D.** 2008. Expression of green fluorescent protein fused to magnetosome proteins in microaerophilic magnetotactic bacteria. Appl. Environ. Microbiol. **74:**4944–4953.
24. **van Heel M, Gowen B, Matadeen R, Orlova EV, Finn R, Pape T, Cohen D, Stark H, Schmidt R, Schatz M, Patwardhan A.** 2000. Single-particle electron cryo-microscopy: towards atomic resolution. Q. Rev. Biophys. **33:**307–369.
25. **Pan Y, Petersen N, Winklhofer M, Davila A, Liu Q, Frederichs T, Hanzlik M, Zhu R.** 2005. Rock magnetic properties of uncultured magnetotactic bacteria. Earth Planet. Sci. Lett. **237:**311–325.
26. **Moskowitz BM, Frankel RB, Bazylinski DA.** 1993. Rock magnetic criteria for the detection of biogenic magnetite. Earth Planet. Sci. Lett. **120:** 283–300.
27. **Li J, Pan Y, Chen G, Liu Q, Tian L, Lin W.** 2009. Magnetite magnetosome and fragmental chain formation of *Magnetospirillum magneticum* AMB-1: transmission electron microscopy and magnetic observations. Geophys. J. Int. **177:**33–42.
28. **Lin W, Pan Y.** 2009. Uncultivated magnetotactic cocci from Yuandadu park in Beijing, China. Appl. Environ. Microbiol. **75:**4046–4052.
29. **Rioux J-B, Philippe N, Pereira S, Pignol D, Wu L-F, Ginet N.** 2010. A second actin-like MamK protein in *Magnetospirillum magneticum* AMB-1 encoded outside the genomic magnetosome island. PLoS One **5:**e9151. doi:10.1371/journal.pone.0009151.
30. **Kruiver PP, Dekkers MJ, Heslop D.** 2001. Quantification of magnetic coercivity components by the analysis of acquisition curves of isothermal remanent magnetisation. Earth Planet. Sci. Lett. **189:**269–276.
31. **Özdemir Ö, Dunlop DJ, Moskowitz BM.** 1993. The effect of oxidation on the Verwey transition in magnetite. Geophys. Res. Lett. **20:**1671–1674.
32. **Butler RF.** 1972. Natural remanent magnetization and thermomagnetic properties of the Allende meteorite. Earth Planet. Sci. Lett. **17:**120–128.
33. **Smirnov AV.** 2006. Low-temperature magnetic properties of magnetite using first-order reversal curve analysis: implications for the pseudo-single-domain state. Geochem. Geophys. Geosyst. **7:**Q11011. doi:10.1029/2006GC001397.
34. **Bazylinski D, Lefèvre C, Schüler D.** 2013. Magnetotactic bacteria, p 453–494. *In* Rosenberg E, DeLong E, Lory S, Stackebrandt E, Thompson F (ed), The prokaryotes. Springer, Heidelberg, Germany.
35. **Schüler D, Köhler M.** 1992. The isolation of a new magnetic spirillum. Zentralbl. Mikrobiol. **147:**150–151.
36. **Fischer H, Mastrogiacomo G, Loffler JF, Warthmann RJ, Weidler PG, Gehring AU.** 2008. Ferromagnetic resonance and magnetic characteristics of intact magnetosome chains in *Magnetospirillum gryphiswaldense*. Earth Planet. Sci. Lett. **270:**200–208.